A numerical study of process complexity in permafrost dominated regions

Radhakrishna Bangalore Lakshmiprasad[1], Fan Zhang[2], Ethan T Coon[3], and Thomas Graf[1,*]

[1]Institute of Fluid Mechanics and Environmental Physics in Civil Engineering, Faculty of Civil Engineering and Geodetic Science, Leibniz Universität Hannover, Hannover, Germany
[2]Key Laboratory of Tibetan Environment Changes and Land Surface Processes, Institute of Tibetan Plateau Research, Chinese Academy of Sciences (CAS), Beijing, China
[3]Climate Change Science Institute and Environmental Sciences Division, Oak Ridge National Laboratory, Oak Ridge, Tennessee, USA

Correspondence: Radhakrishna Bangalore Lakshmiprasad (radhakrishna@hydromech.uni-hannover.de)

Abstract.

Numerical modeling of permafrost requires adequate representation of atmospheric and surface processes, a reasonable parameter estimation strategy, and site-specific model development. The three main research objectives of the study are: (i) to propose a methodology that determines the required level of surface process complexity of permafrost models, (ii) to design and compare different conceptual numerical models of increasing surface process complexity, and (iii) to calibrate and validate the numerical models setup at the Yakou catchment on the Qinghai-Tibet Plateau. Three cases with varying top boundary conditions have been established: (i) Case 1: Dirichlet thermal boundary condition of measured surface temperature at 0.0 m. (ii) Case 2: Surface water and energy balance without snow. (iii) Case 3: Surface water and energy balance with snow. The calibration was carried out by coupling the Advanced Terrestrial Simulator (Numerical model) and PEST (Calibration tool). Simulation results showed that (i) Permeability and Van Genuchten alpha of peat and mineral were highly sensitive. (ii) The thawing of permafrost was not adequately represented by considering only subsurface processes. (iii) Liquid precipitation aided in increasing the rate of permafrost degradation. (iv) Deposition of snow insulated the subsurface during the thaw initiation period. We have successfully established a pseudo-1-D model at the Yakou catchment in the QTP. A novel methodology is proposed to assess the surface process level complexity in permafrost-dominated regions. The numerical model can be used to determine the impacts of climate change on permafrost degradation.

Keywords: Permafrost, numerical modeling, calibration, Qinghai Tibet Plateau.

1 Introduction

The Qinghai-Tibet Plateau (QTP), also known as the "Water Tower of Asia", is threatened by climate change (Chang et al., 2018). The influence of climate change is more significant at high elevations, and warming and wetting trends are expected to continue in the coming decades (Stocker, 2014). Due to the high elevation of the QTP (average 4000 m.a.s.l), the rate of temperature increase is twice the global average (Xiao et al., 2020b). Increasing temperature leads to permafrost degradation

on the QTP (Xiao et al., 2020b). Permafrost degradation leads to drastic changes in the biogeohydrochemical cycles. A few impacts of permafrost degradation on the QTP are summarised here: Zhang et al. (2017) found that 12% of the increase in lake water and groundwater storage was attributed to permafrost thaw. Also, permafrost-degraded regions in the Xidatan area

25   of the QTP were affected by vegetation deterioration (Yue et al., 2013). Large soil organic carbon and nitrogen stocks were drastically reduced with permafrost degradation mainly due to soil water content variation in the western parts of the QTP (Wu et al., 2016). Hence, it is crucial to better understand permafrost dynamics.

    The term permafrost is defined by the International Permafrost Association (IPA) as "ground (soil or rock) that remains at or below 0°C for two or more consecutive years" (S.A. Harris, 1998). The top layer of the subsurface that thaws during

30   summer and freezes again in autumn is called the active layer. The active layer is the water-saturated zone below the vadose zone. The active layer plays a decisive role in hydrological, ecological, and biochemical processes between the atmosphere and the subsurface (Kane et al., 1991). The active layer is the critical zone for heat transport because heat is transferred from the ground surface to the permafrost through this zone (Langford et al., 2020). Therefore, the active layer in the QTP has received international attention (Zhou et al., 2013). The critical factors influencing active layer depth are air temperature, solar radiation,

35   vegetation, soil moisture, snowfall duration and intensity, thermal properties of soil, and the near-surface organic layer (Zhou et al., 2013). The change in active layer depth modifies the subsurface groundwater distribution, porosity, permeability, thermal conductivity, and heat capacity (Chang et al., 2018). Modeling the active layer dynamics with the changing atmospheric, surface, and subsurface conditions will provide insight into the future state of permafrost.
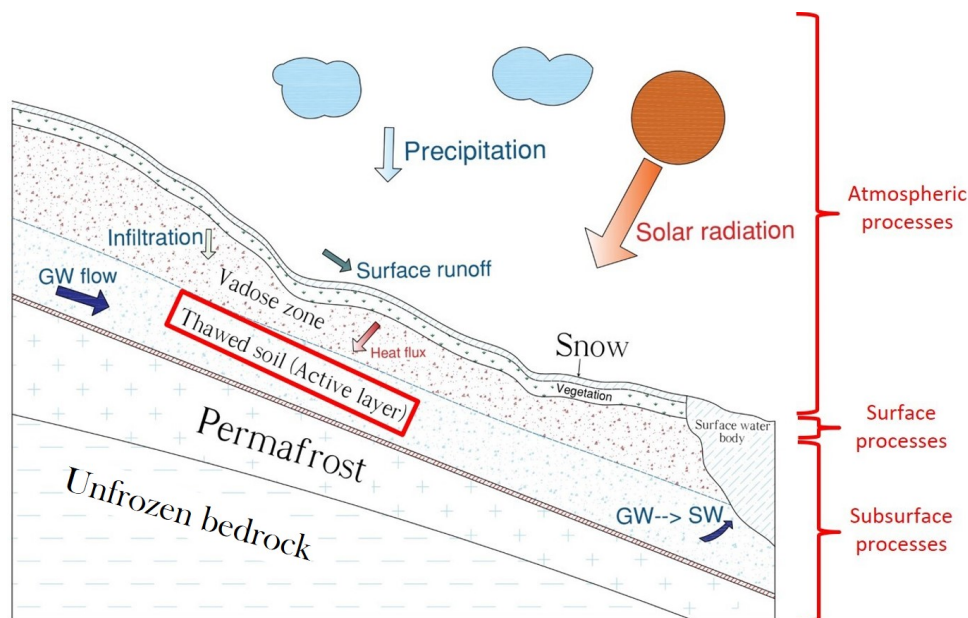
Figure 1. Conceptual diagram depicting the physical components and the processes associated with permafrost-dominated regions. The processes can be broadly classified into atmospheric (precipitation and solar radiation), surface (snow dynamics, evapotranspiration, and surface runoff), and subsurface (thawing and freezing of permafrost) processes. The hydraulic and thermal fluxes are represented in blue and red arrows, respectively.

The conceptual diagram shown in Figure 1 depicts the cryohydrogeological processes involved at the hillslope scale. The
40   processes can be classified into atmospheric, surficial, and subsurficial processes. The atmospheric processes are precipitation and solar radiation, which are the main drivers of surficial and subsurficial processes. The surficial processes include snow dynamics, evapotranspiration, and surface runoff, which are mainly influenced by land and soil types. The subsurface processes mainly include the thawing and re-freezing of permafrost. The subsurface states from the top to bottom include the vadose zone, active layer, permafrost, and unfrozen bedrock. The freezing front at the permafrost table separates the permafrost from the
45   active layer. Unfrozen bedrock with very low hydraulic conductivity is assumed to occur below the permafrost base. The atmosphere, surface, and near-subsurface interactions govern the permafrost dynamics.

The surface water and energy balance components determine the permafrost dynamics in the subsurface. Precipitation and snow melt are important hydraulic inputs to drive the surface and subsurface hydrological processes. During rainfall, increased surface runoff and evapotranspiration occur based on topography and surface conditions. During winter, snowfall accumulates
50   on the surface, which acts as an insulation layer to prevent cold air temperatures from reaching the subsurface, thereby keeping the frozen subsurface warmer than the atmosphere. During the spring-summer transition period, snowmelt provides additional hydraulic input to the subsurface. Surface energy fluxes drive the energy balance, including incoming and outgoing shortwave and longwave radiation, latent heat of evaporation, sensible heat flux, and heat conduction through the snowpack. The degree of surface process complexity is determined by the climatic conditions in the study area.

55   There is a continuous exchange of heat and water fluxes between the surface and subsurface. These fluxes determine the subsurface hydraulic and thermal states. The soil moisture in the vadose zone and the active layer are influenced by the hydraulic fluxes. Heat transport within the subsurface is controlled mainly by conduction due to a temperature gradient (McKenzie et al., 2007). The lateral inflow of warm groundwater through the active layer induces advective heat transport that can accelerate permafrost thaw (Dagenais et al., 2020b; Albers et al., 2020a; Voss and Provost, 2010), given there is sufficient flow of water.

60 Latent heat is absorbed or released in the active layer due to dynamic subsurface thawing or freezing, respectively. The thermal influence on the permafrost base is controlled by the geothermal gradient. Freezing and thawing of the subsurface lead to changes in thermal and hydraulic properties. As the temperature decreases, the water freezes, and latent heat is released. The thermal conductivity of ice is approximately four times that of water, and the specific heat capacity of ice is half that of water (McKenzie et al., 2007). Thus, the specific heat capacity decreases, and the thermal conductivity increases due to an

65 increase in ice saturation. As the ice saturation increases, porosity, permeability, density, and hydraulic conductivity decrease. This shows that groundwater flow and heat transport are physically coupled due to the interrelationship between parameter values. Numerical modeling is an effective method to assess atmosphere-surface-subsurface interaction in permafrost-dominated regions.

    From a cryosphere perspective, the interest in permafrost hydrology is relatively recent compared to glacier and snow

70 hydrology (Yongjian et al., 2020). From a global perspective, the literature on permafrost dynamics in the QTP (high elevation and dry climate) compared to Arctic regions (low elevation and wet climate with coastal influence) is also relatively new and scarce (Gao et al., 2021), but a few cryohydrogeological [CHG] models have been applied in the QTP. The CHG models applied in the QTP can be classified into physically based freeze-thaw models and catchment scale permafrost runoff models (Gao et al., 2021). The physically based freeze-thaw models require an adequate representation of ice and surface processes. Additionally,

75 parameter information and calibration datasets are essential to adjust the model conditions to the field site.

    A few of the applied physically based freeze-thaw models are listed here: The 1-D CoupModel was employed to simulate and compare the soil temperature, moisture, and heat flux with the measured values at the Tanggula station (Central region of QTP) (Hu et al., 2015). Independent subsurface flow and thermal transport equations without phase change and a surface energy balance equation were considered. CoupModel was applied at the Tanggula station to investigate the influence of snowpack

80 and organic soil on the active layer depth (Zhou et al., 2013). The same processes as in Hu et al. (2015) were considered by Zhou et al. (2013), along with snow conduction and snow melt. Manual calibration was carried out with Nash Sutcliffe Efficiency (NSE), Root Mean Square Error (RMSE), and Mean Error (ME) as the evaluators to compare the simulated and measured snow depth, heat flux, and near-surface temperature values. Huang et al. (2020b) used the FEFLOW-ICE simulator to identify the impacts of spatiotemporal variations in land surface temperature caused by topography on suprapermafrost

85 groundwater systems in Fenghoushan watershed (Huang et al., 2020b). FEFLOW-ICE simulates ice content by coupling the flow and heat transport equations through empirical methods. Manual calibration of porosity and permeability was carried out with RMSE, NSE coefficient, and coefficient of determination (R^2) as evaluators. Zhang et al. (2016) employed COMSOL to

design a conceptual CHG model in the Beiluhe region that considers the coupled processes of subsurface flow, subsurface heat transport, surface water, and surface energy balance. The model was manually calibrated and validated with the measured soil heat flux, temperature, and volumetric water content (VWC). In conclusion, the level of surface process complexity, parameter estimation strategy, and field application procedure in most cryohydrogeological (CHG) models need to be thoroughly justified.

The three main research objectives of the present study are: (i) to establish a methodology that determines the required level of surface process complexity of permafrost models, (ii) to design and compare different conceptual CHG models of increasing surface process complexity, and (iii) to calibrate and validate the conceptual CHG models for a given catchment on the QTP. The Advanced Terrestrial Simulator (ATS) and the Parameter ESTimation (PEST) tool were chosen as the numerical model and calibration tool, respectively.

2   Materials and Methods

2.1   Advanced Terrestrial Simulator (ATS)

The Advanced Terrestrial Simulator (ATS) is an ecosystem-based, integrated, and distributed hydrology code that can model hydro-thermal surface-subsurface processes: surface energy and water balance processes with snow deposition/melting; overland energy and flow processes; subsurface energy and flow processes (Painter et al., 2016). ATS is based on a multiphysics process model management system (Coon et al., 2016) derived from the Amanzi code (Moulton et al., 2012). ATS is one of the few integrated CHG models that can simulate coupled surface-subsurface processes with phase change of water in variably saturated soils and uses physically based equations for the coupling (Lamontagne-Hallé et al., 2020). ATS has been verified in the Interfrost CHG benchmarking initiative (Grenier et al., 2018) and tested and applied with several field datasets mainly in arctic regions, e.g. Frampton et al. (2013); Atchley et al. (2015); Harp et al. (2016); Jafarov et al. (2018, 2020). Additionally, ATS can also model plant dynamics, mechanical deformation, reactive transport, and carbon cycle dynamics.

The processes and respective equations considered in this article are outlined in the appendix A. ATS first solves the above-surface energy and water balance equations, then the overland energy and flow equations, and finally the subsurface energy and flow equations (Painter et al., 2016). The two primary unknowns governing the thermal and hydrological processes are temperature and pressure, respectively.

2.2   Conceptual model

Figure 2 shows the conceptual models of the three cases of increasing surface process complexity. The three models are based on the typical surface boundary conditions that are selected from previous literature for permafrost domains. The main goal of selecting the three cases was to compare the level of permafrost process representation and select the appropriate case that represents the environmental conditions in the study area. A pseudo-1-D model of 40 m depth and unit cross-sectional area
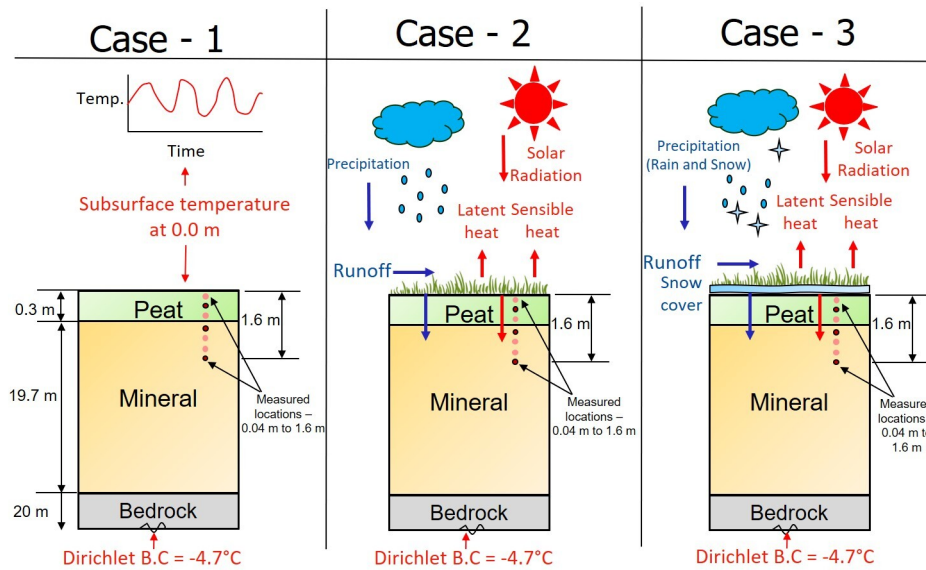
Figure 2. Pictorial representation of the top boundary conditions, surface water and energy fluxes, subsurface mesh, and measured locations for the three cases.

was chosen. ATS simulates processes in a three-dimensional domain, therefore the model is provided with a unit surface area. The 1-D model consists of three layers: Peat (0 m - 0.3 m), mineral layer (0.3 m - 20 m), and unfrozen bedrock (20 m - 40 m). There are 400 cuboidal cells, each with the dimensions 1 m X 1 m X 0.1 m (length X breadth X depth). The method for

120 processing and interpreting the input datasets is provided in the appendix (Section B). Table 1 provides the conditions taken for spinup, calibration, validation, and final simulation.

Typical cases: The conceptual model considers three cases where the domain top is represented differently with increasing process complexity for each case: (i) Case 1: Dirichlet thermal boundary condition of measured surface temperature at 0.0 m. (ii) Case 2: Surface water and energy balance without snow. (iii) Case 3: Surface water and energy balance with snow. Case 2

125 and Case 3 calculate the water and energy fluxes along the surface. For all cases, the bottom boundary condition of temperature is -4.7°C, and a seepage face head of 0.015 m allows lateral surface runoff.

Spinup: An initial condition can be determined using measured data or by conducting a spinup. The initial conditions were generated with spinup simulations because measured data was only available for temperature and saturation until 1.6 m depth. Spinup is a two-step procedure that involves both static and dynamic spinup. Scenario 0 represents the static spinup for all

130 three cases, and Scenarios I, II, and III represent the dynamic spinup for Cases 1, 2, and 3, respectively.

Static spinup - Scenario 0: The main goal of static spinup is to gradually freeze the column from below and serve as the initial condition for the dynamic spinup. Only subsurface processes are considered for the static spinup. The initial hydraulic conditions are assigned based on the depth of the water table from the surface. The results are compared with different values

for the initial depth to water table: -0.5, -0.8, -1, -1.2, -1.6, -5, and -10 m, and it was seen that -1 m was most suitable after

135 comparing with the field data. We assumed the initial temperature of -4.7°C, which is the average air temperature at the Yakou catchment. The bottom thermal boundary condition is linearly decreasing temperature from 0.5°C to -4.7°C from 0 to 1000 days, thereby slowly freezing the column from the bottom. There is a no-flow boundary condition on the top of the domain. The simulation took 100 years to achieve a quasi-steady state.

Dynamic spinup - Scenarios I, II, III: The dynamic spinup simulates a transient cyclic state, which serves as the initial

140 condition for the actual simulation (Cases 1, 2, 3). The top boundary condition for the three scenarios remains the same for the three typical cases. The initial conditions for the three scenarios are assigned from the steady state of the static spinup. The top boundary condition is assigned with cyclic average data: daily average calculated for all years from 2016 to 2020 to produce a single-year dataset. Then, this data is replicated nine times to generate a ten-year input dataset. Note that we had access to only two years (2016, and 2017) of the snow depth data, which was used to prepare the cyclic average data. The simulation time

145 was taken as ten years to achieve a quasi-steady state. The quasi-steady state condition was checked by determining the daily difference between the current and previous year. The difference was close to zero for soil temperature, saturation of liquid, saturation of ice, and saturation of gas at vertical depths 0.8 m, 1.6 m, 5.0 m, 10.0 m, and 40.0 m after ten years.

Calibration and Validation: The physical processes and boundary conditions considered for the calibration and validation remain the same for the typical cases. The initial subsurface conditions of pressure and temperature for Case 1, Case 2, and

150 Case 3 are assigned from the final state of the three dynamic spinup scenarios I, II, and III, respectively. The initial surface conditions for Case 2 and Case 3 are assigned from the final temperature and hydraulic head of the top of the subsurface from scenarios II and III, respectively. For Case 1 and Case 2, three years (2016-2018) were considered for calibration and one year for validation (2019). For Case 3, one year (2016) was chosen for calibration and one year (2017) for validation. The calibrated parameters are used for the validation simulations.

155 **Final simulation:** The final simulation is conducted to interpret the results and compare the three cases. The conditions for the final simulation are the same as for validation, except that the cyclic average data of one year is used.

2.3 Calibration tool - Parameter ESTimation (PEST)

PEST is a calibration and uncertainty analysis software package for numerical models to improve environmental model-based decisions. PEST has previously been coupled with the CHG models HEATFLOW (Albers et al., 2020b; Dagenais et al., 2020a),

160 and ATS (Atchley et al., 2015; Harp et al., 2016; Jafarov et al., 2020). Based on a measured dataset, PEST calibration uses a Bayesian approach to determine the most suitable parameter sets. The Gauss Levenberg Marquardt (GLM) algorithm from PEST suites is chosen here for the calibration analysis. The objective function (ϕ_{min}) is a sum of the mean square error of temperature and saturation multiplied by its corresponding objective weights (w_t for temperature, w_s for VWC):

Table 1. Spinup, calibration, and validation conditions: goals, processes, initial conditions, boundary conditions, input data, and simulation time for Scenarios (I, II, III, and IV) and Cases (1, 2, and 3).

Scenarios and Cases		Scenario I (Case 1 static spinup)	Scenario II (Case 1 dynamic spinup) and Case 1	Scenario III (Case 2 dynamic spinup) and Case 2	Scenario IV (Case 3 dynamic spinup) and Case 3
Scenario goals		- To freeze the column from the bottom. - Initial conditions for the dynamic spinup.	- It sets the typical transient cyclic state for the subsurface. - Initial condition for Case 1.	- It sets the typical transient cyclic state. - Initial condition for Case 2.	- It sets the typical transient cyclic state. - Initial condition for Case 3.
Processes		Subsurface processes - Coupled mass and energy transport equation.	Subsurface processes - Coupled mass and energy transport equation.	Subsurface processes + Surface energy and water balance without snow	Subsurface processes + Surface energy and water balance with snow.
Initial conditions	Subsurface thermal	-4.7°C.	Initial conditions from the final state of scenario I for scenario II and scenario II for Case 1	Initial conditions from the final state of scenario I for scenario III and scenario III for Case 2.	Initial conditions from the final state of scenario I for scenario IV and scenario IV for Case 3.
	Subsurface hydraulic	Hydrostatic head: Depth to water table from the surface is -1.0 m.	Initial conditions from the final state of scenario I for scenario II and scenario II for Case 1.	Initial conditions from the final state of scenario I for scenario III and scenario III for Case 2.	Initial conditions from the final state of scenario I for scenario IV and scenario IV for Case 3.
	Surface thermal	-	-	Initializing temperature from subsurface (at 0.0 m) final state of scenario I for scenario III and scenario III for Case 2.	Initializing temperature from subsurface (at 0.0 m) final state of scenario I for scenario IV and scenario IV for Case 3.
	Surface hydraulic	-	-	Initializing head from subsurface (at 0.0 m) final state of scenario I for scenario III and scenario III for Case 2.	Initializing head from subsurface (at 0.0 m) final state of scenario I for scenario IV and scenario IV for Case 3.
Boundary conditions	Subsurface thermal	Bottom: Linear temperature variation from 0.5°C to -4.7°C from 0 to 1000 days.	Top: Cyclic average subsurface temperature at 0.0 m; Bottom: -4.7°C.	Top: Surface energy balance input as energy flux; Bottom: -4.7°C	Top: Surface energy balance input as energy flux; Bottom: -4.7°C.
	Subsurface hydraulic	-	-	Top: Surface water balance input as mass flux; Bottom: -4.7°C	Top: Surface water balance input as mass flux; Bottom: -4.7°C.
	Surface thermal	-	-	Surface energy balance flux	Surface energy balance flux.
	Surface hydraulic	-	-	Surface water balance mass flux; Seepage face head at surface = 0.015 m	Surface water balance mass flux; Seepage face head at surface = 0.015 m.
Input data		-	Cyclic average subsurface temperature at 0.0 m.	Cyclic average air temperature, relative humidity, incoming shortwave radiation, liquid precipitation, wind speed.	Cyclic average air temperature, relative humidity, incoming shortwave radiation, liquid precipitation, wind speed, solid precipitation.
Simulation time - Scenarios (S), Calibration (C), Validation (V)		100 years - until steady state is reached (S).	10 years - initiate repeated thawing and freezing until steady state (S); three years from 2016 to 2018 (C); 1 year for 2019 (V).	10 years - initiate repeated thawing and freezing until steady state (S); three years from 2016 to 2018 (C); 1 year for 2019 (V).	10 years - initiate repeated thawing and freezing until steady state (S); 1 year for 2016 (C); 1 year for 2017 (V).

$$\phi_{min} = w_t \sum_{i}^{n_{depth}} \sum_{i}^{n_{days}} (T_{mj}^i - T_{sj}^i)^2 + w_s \sum_{i}^{n_{depth}} \sum_{i}^{n_{days}} (S_{mj}^i - S_{sj}^i)^2 \tag{1}$$

165   where n_{depth} [m] represents the vertical depths of the measurement and n_{days} represents the number of days considered for the calibration. T_m [°C] and T_s [°C] are the measured and simulated subsurface temperature values, respectively, and S_m [-] and S_s [-] are the measured and simulated VWC values, respectively.

     We coupled PEST with the numerical code ATS to calibrate the parameters. The parameters for calibration for the three cases are shown in Table 4. Case 1 had 21 parameters, whereas Case 2 and Case 3 had 12 parameters each for calibration. An initial

170 round of manual parameter sensitivity analysis showed that unfrozen bedrock parameters had no sensitivity and, therefore, were not considered in the PEST calibration analysis. The parameters chosen are given in Table A1. The total number of observations used in Case 1 and Case 2 is 15344 values, including subsurface temperature and VWC at seven depths (0.04, 0.1, 0.2, 0.4, 0.8, 1.2, and 1.6 m) for three years. For Case 3, we used 5124 observation values, which are the same as mentioned above, but for one year. The calibration data was measured at the Yakou meteorological station, and further information is provided

175 in the appendix (Section B). The number of observations greatly surpasses the number of parameters in the objective function; hence, we can consider it to be a "well-posed inverse problem" (Doherty, 2015). PEST software utility program (pwtadj1) was employed to adjust the individual observation weights such that each observation group (temperature and VWC) had the same influence in the calibration analysis (Doherty, 2015).

2.4 Validation

180 The input dataset for Case 1 and Case 2 was one year (2019), and for Case 3, also one year (2017). The parameters considered for the validation are the calibrated parameters determined using the Gauss Levenberg Marquardt (GLM) algorithm as described in section 2.3. The initial and boundary conditions for the three cases remain the same as the calibration analysis(Section 2.2). The Nash-Sutcliffe Efficiency (NSE) coefficient was used to assess the model performance. It is given by the equation (Huang et al., 2020b):

$$185 \quad NSE = 1 - \frac{\sum_{t=1}^{T}(V_o^t - V_m^t)^2}{\sum_{t=1}^{t_f}(V_o^t - \bar{V}_o)^2} \tag{2}$$

Here, t_f [days] is the final time, V_o^t [°C or -] is the observed variable (Temperature or VWC), V_m^t [°C or -] is the modeled variable which varies with time t [days], and $\bar{V}_o$ [°C or -] is the mean of the observed variable. The perfect model has an NSE value of 1. If the value of NSE is less than 0, the observed mean of the time series is a better predictor of the model.

2.5 Study area

190 The study area is the Yakou catchment located on the North-Eastern tip of the QTP with a relatively small area of 1.4 km^2 (Figure 3). The Yakou catchment is one of the well-investigated upstream catchments in the Heihe River basin. It experiences a continental climate with a mean air temperature of -4.7°C and mean annual precipitation of 405 mm (based on measured data from January 2014 - December 2017 at the Yakou meteorological station). It is a south-facing catchment that experiences relatively low snow cover during the winter. It has an average elevation of 4050 m (3900 m - 4300 m). Due to its high altitude

195 and low snow cover, the Yakou catchment is located in the continuous permafrost zone. The catchment is divided into the up-slope, middle-slope, and riparian zones based on elevation and vegetation. The Yakou meteorological station is located in the up-slope zone, which has been measuring data since 2015 (Xiao et al., 2020b). Further information about the meteorological data used is provided in the appendix (Section B).

The main surface types for the up-slope, middle-slope, and riparian zones are the alpine desert, alpine meadow, and alpine

200 swamp meadow, respectively. The percentage of vegetation cover increases from 60% to 98% from the up-slope to the riparian zone. The up-slope experiences a steep slope of about 20° and reduces gradually to 7° in the riparian zone. The soil types of the up-slope, middle-slope, and riparian zones are cryogenic Cambisols, mat-cryic Cambisols, and organic cryic Gleysols, respectively. The near-subsurface properties exhibit a sod layer and humus layer at 0-30 cm depth and a leached and illuvial layer at 30 - 60 cm depth. The dominant soil type is fine-grained silty sand and clay (>65%) (Xiao et al., 2020a). The 1-D

205 numerical model was established in the up-slope; therefore, we consider these properties for the model development.
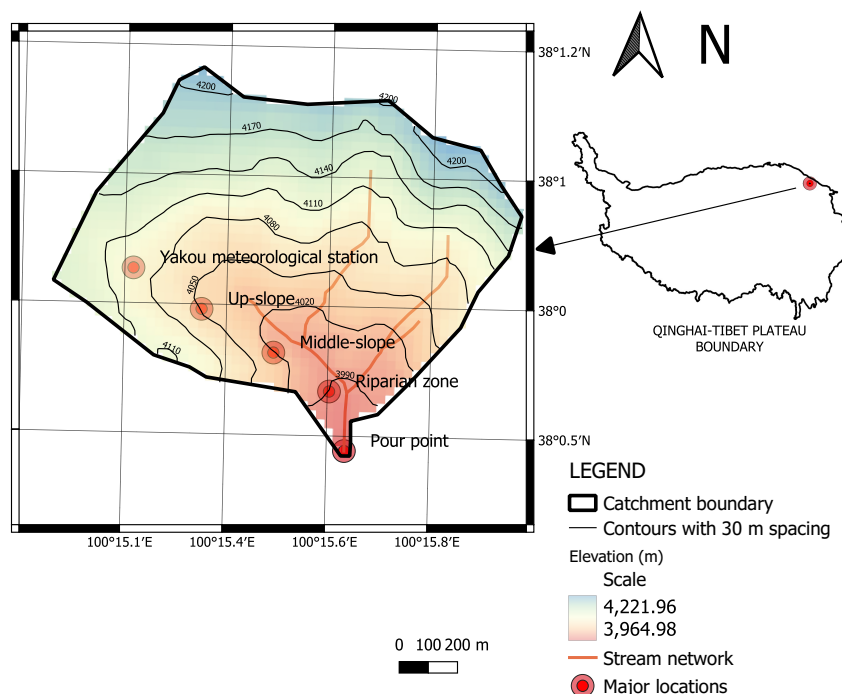
Figure 3. Location of Yakou catchment on the northeastern Tibetan Plateau shown on the right. The digital elevation model and catchment features are shown on the left. The QTP boundary and the digital elevation dataset was taken from Ran et al. (2020) and Farr et al. (2007), respectively.

The suprapermafrost dynamics in the Yakou catchment can be divided into four periods (Chang et al., 2015): (i) Completely frozen period (January - April): The water in the soil is completely frozen due to low temperatures, such that the VWC is very low. (ii) Thaw initiation period (May - June): The permafrost begins to thaw at the surface due to increased air temperature and is represented by a corresponding increase in the VWC with increasing depth. (iii) Thawed period (July - September): The

210 permafrost thaw continues until the active layer reaches its maximum thaw depth. (iv) Freeze initiation period (October - December): The air temperature drops below 0°C, which initiates downward freezing within the subsurface and a corresponding decrease of the VWC with depth. The hydraulic and thermal processes occurring in the atmosphere mainly control the length of the four periods. The periods were decided based on the weather station dataset, subsurface temperature, and VWC datasets available at the Yakou meteorological station from 2015 to 2020.

3 Results and discussion

3.1 Calibration

The comparison of three cases based on the results from the PEST calibration analysis comprises three parts: (i) input and calibration requirements, (ii) residuals – the difference between the measured and simulated values, and (iii) calibrated parameters. Case 1 initially had all the parameters for calibration. Based on the results from Case 1 calibration, the very low sensitive parameters were removed in Case 2 and Case 3 calibration analysis.

Table 2 gives the input datasets and calibration requirements. The number of input datasets and parameters is greater for Case 2 and Case 3 than for Case 1. The calibration time is the highest for Case 2 and lowest for Case 3 because Case 2 required more model runs to achieve the least objective function. The time taken for each model run depends on the convergence of the numerical model at each time step. Although Case 1 ran 167 model runs, it required nearly twice the total simulation time compared to Case 3. The reason can be that (i) Case 2 was tested with more calibration parameters than Case 3, (ii) Case 3 represents all the processes similar to reality; hence, Case 3 simulates values close to the measured values. As given by the equation 1, the final objective function value varied from low to high from Case 2 to Case 1 to Case 3. A lower objective function value represents a better match of the simulation results with respect to the measured values. This means that Case 2 performs best in achieving the lowest objective function value. However, Case 2 requires more data, more parameters, and longer simulation times. Case 1 has the second lowest objective function value and requires the fewest parameters.

Table 2. Input and calibration requirements for the three cases.

	Cases/Conditions	Case 1	Case 2	Case 3
Input	Data requirement	Near subsurface temperature	Incoming shortwave radiation, air temperature, relative humidity, wind speed, and liquid precipitation	Incoming shortwave radiation, air temperature, relative humidity, wind speed, liquid precipitation, and solid precipitation
	Number of Parameters	21	27	27
Calibration	Number of parameters to calibrate	21	12	12
	Number of model runs	167	452	237
	Total simulation time (hours)	10.021	35.96	5.30
	Final objective function value	0.0031	0.0026	0.0072
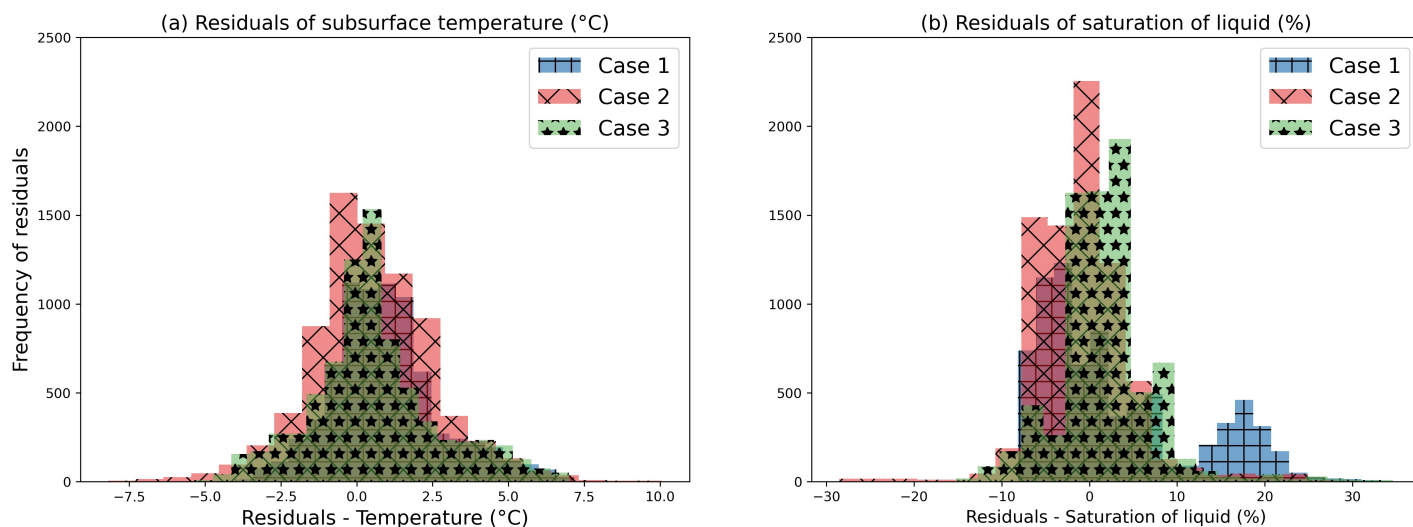
Figure 4. A histogram plot of the residuals for (a) subsurface temperature and (b) liquid saturation from the calibration analysis for the three cases.

Table 3. The mean and standard deviation of the residuals of subsurface temperature and liquid saturation for the three cases.

	Temperature (°C)		Liquid saturation (%)	
	Mean	Standard deviation	Mean	Standard deviation
Case 1	0.961	1.821	3.094	8.874
Case 2	0.474	2.043	-0.832	5.59
Case 3	0.573	2.108	1.781	5.581

Figure 4 shows the histogram plot of the residuals; the mean and standard deviation are given in Table 3. The residuals are calculated by subtracting the measured from the simulated values. The mean residual temperature values show that Case 3 has the lowest value compared to Case 2 and Case 1; however, Case 3 has the highest standard deviation. Due to the inclusion of snow in Case 3, the subsurface experiences a zero-curtain effect during the thaw and freeze initiation periods. Therefore, the
235 mean subsurface temperature (around 0 °C) is adequately observed. The zero-curtain effect is typical in permafrost-dominated regions where the phase change between water and ice is retarded due to latent heat release (Jiang et al., 2012). Case 2, on the other hand, has a mean of 0.474 °C and a standard deviation of 2.043 °C. The surface-subsurface heat flux is well-represented in Case 2, mainly during the thawing period. The temperature residual values of Case 1 also range about zero with a smaller spread than Case 2 because the subsurface temperature at 0.0 m is the top boundary condition in Case 1.
240 Regarding predicting the liquid saturation, Case 2 has a residual mean of -0.832 and a standard deviation 5.59. The liquid saturation residuals for Case 2 vary around zero, with a smaller spread on both sides. Case 3 has a slightly larger residual liquid saturation value than Case 1 because snow deposition delays the thaw initiation period and the increase in liquid saturation.

The liquid saturation residual values have two peaks for Case 1, which can be due to the inability to predict the liquid saturation during the frozen and thawing periods. Case 2 is found to be the most suitable of all three cases.
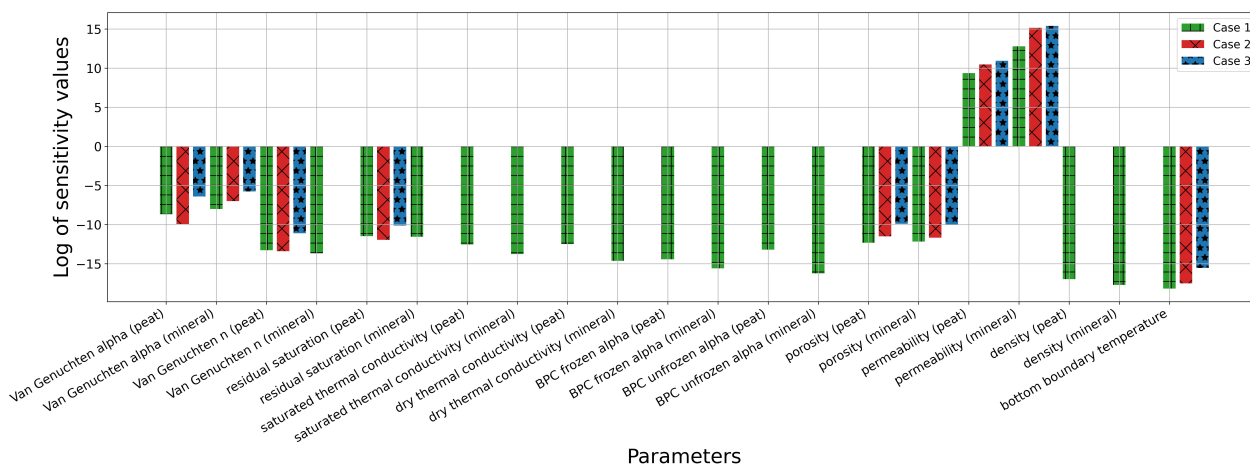
Figure 5. The log of parameter sensitivity values for the three cases from the PEST calibration analysis.

Table 4. The log of parameter sensitivity values for the three cases and the corresponding ranking from the PEST calibration analysis.

	Case1	Case1-rank	Case2	Case2-rank	Case3	Case3-rank
Permeability (mineral)	12.7851	1.0	15.1567	1.0	15.413	1.0
Permeability (peat)	9.379	2.0	10.4848	2.0	10.9437	2.0
Van Genuchten alpha (mineral)	-8.0047	3.0	-6.9986	3.0	-5.757	3.0
Van Genuchten alpha (peat)	-8.6714	4.0	-9.9138	4.0	-6.390	4.0
Residual saturation (peat)	-11.4619	5.0	-11.9317	7.0	-10.127	7.0
Residual saturation (mineral)	-11.5402	6.0	-	-	-	-
Porosity (mineral)	-12.156	7.0	-11.6707	6.0	-10.034	6.0
Porosity (peat)	-12.2997	8.0	-11.4837	5.0	-9.883	5.0
Dry thermal conductivity (peat)	-12.4895	9.0	-	-	-	-
Unfrozen saturated thermal conductivity (peat)	-12.5177	10.0	-	-	-	-
BPC unfrozen unsaturated alpha (peat)	-13.1899	11.0	-	-	-	-
n (peat)	-13.2709	12.0	-13.404	8.0	-11.113	8.0
n (mineral)	-13.6529	13.0	-	-	-	-
Unfrozen saturated thermal conductivity (mineral)	-13.7549	14.0	-	-	-	-
BPC frozen unsaturated alpha (peat)	-14.431	15.0	-	-	-	-
Dry thermal conductivity (mineral)	-14.6124	16.0	-	-	-	-
BPC frozen unsaturated alpha (mineral)	-15.5834	17.0	-	-	-	-
BPC unfrozen unsaturated alpha (mineral)	-16.2356	18.0	-	-	-	-
Density (peat)	-16.9615	19.0	-	-	-	-
Density (mineral)	-17.7084	20.0	-	-	-	-
Bottom boundary condition	-18.1781	21.0	-17.496	9.0	-15.546	9.0

Table 5. The calibrated parameters for all cases, literature parameter values (O'Connor et al. (2020)) and parameters based on experience for the soil type (cryogenic cambisols with a high percentage of clay) at the Yakou catchment up-slope.

Parameters	Calibrated parameters				
	Case 1	Case 2	Case 3	O'Connor et al. (2020)	From experience
Van Genuchten alpha (peat)	0.0025	0.0112	0.0025	0.0353	0.01 - 0.05
Van Genuchten alpha (mineral)	0.0018	0.0005	0.0011	0.001	10^{-4} - 0.007
Van Genuchten n (peat)	2.049	1.487	1.4682	1.5137	1.0 - 2.0
Van Genuchten n (mineral)	2.05	2.0348	1.4846	1.5137	1.5 - 2.5
Residual saturation (peat)	0.2278	0.1789	0.1347	0.0467	0.1 - 0.2
Residual saturation (mineral)	0.1617	0.2767	0.1561	0.0467	0.1 - 0.25
Unfrozen saturated thermal conductivity (peat)	0.4422	0.7693	0.492	0.67	0.3 - 0.8
Unfrozen saturated thermal conductivity (mineral)	0.9518	0.238	0.9382	1	0.8 - 2.0
Dry thermal conductivity (peat)	0.1036	0.1158	0.1207	0.07	0.03 - 0.12
Dry thermal conductivity (mineral)	0.9842	1.1451	0.9844	0.29	0.25 - 0.5
BPC frozen unsaturated alpha (peat)	1.5051	0.9105	1.4966	1	-
BPC frozen unsaturated alpha (mineral)	1.4994	1.6688	1.4991	1	-
BPC unfrozen unsaturated alpha (peat)	0.4858	0.1217	0.4771	0.5	0.1 - 0.6
BPC unfrozen unsaturated alpha (mineral)	0.6989	1.1554	0.6992	0.5	0.1 - 0.6
Porosity (peat)	0.6383	0.4215	0.4386	0.88	0.5 - 0.9
Porosity (mineral)	0.4816	0.3623	0.3727	0.36	0.2 - 0.5
Permeability (peat)	1.34E-11	1.34E-11	5.60088e-11	1.00E-07	-
Permeability (mineral)	1.75e-13	3.04505e-14	1.75e-13	1.00E-08	-
Density (peat)	900.0	900	900	7.00E+02	600 - 900
Density (mineral)	1900.0	1900	1900	2.17E+03	1900 - 2200
Bottom boundary condition	-4.7	-4.7	-4.7	-	-

245   Figure 5 and Table 4 show the log of sensitivity of the parameters for the three cases. The parameters were classified based on their sensitivity: High - permeability, Van Genuchten alpha (mineral and peat); Medium - residual saturation, the porosity of peat and mineral, and dry thermal conductivity and saturated thermal conductivity of peat; Low - alpha unfrozen of peat, Van Genuchten n of peat and mineral, the saturated thermal conductivity of mineral; and the remaining parameters have a very low or no sensitivity. Parameters of the mineral layer were found, in general, to be more sensitive than those of peat because of the

250   existence of permafrost in the mineral layer. The dynamic change of temperature and VWC is promoted by permafrost. The hydraulic parameters were also more sensitive than thermal parameters, probably due to the uncertainty of VWC estimation compared to the soil temperature estimation. Soil permeability is the most sensitive parameter, which varies by several orders of magnitude due to seasonal thawing and freezing of the subsurface (Huang et al., 2020a; Kurylyk and Watanabe, 2013). The Van Genuchten alpha and residual saturation influence the seasonally varying ice and water content, and both these parameters

255   were found to be sensitive in the study by Schuh et al. (2017). Nonetheless, the Van Genuchten n had low sensitivities, which contradicts the findings from Schuh et al. (2017). The dry and saturated thermal conductivity of peat is affected by the high variation of liquid saturation due to atmospheric influences. Peat and mineral layer density had very low sensitivity because they are neither considered in the subsurface thermal nor hydraulic equations. Albers et al. (2020b) concluded that the near-surface and freezing function parameters show the highest sensitivity, as also seen in our study.

260   The comparison of the calibrated parameters with the literature values is explained in this paragraph (Table 5). For Case 1, the permeability and Van Genuchten alpha value of both peat and mineral are lower than expected, and the residual saturation of peat is slightly higher than expected. For Case 2, the porosity of peat, saturated thermal conductivity, and dry thermal conductivity of mineral are slightly lower than expected. The permeability might be underestimated here because the permafrost layer undergoes repeated thawing and freezing, resulting in the variation of permeability by multiple orders of magnitude (Kurylyk

265   and Watanabe, 2013). For Case 3, the Van Genuchten alpha value and porosity of peat and mineral are lower than expected, and the dry thermal conductivity of mineral, BPC frozen, and unfrozen unsaturated alpha is higher than expected. The Van Genuchten alpha, residual saturation, and BPC alpha are highly soil-specific; hence, it is harder to determine accurately by the numerical model. The underestimation of porosity could be due to the high clay content in the peat layer. The rest of the parameters for all cases are within realistic ranges.

270   ## 3.2   Validation
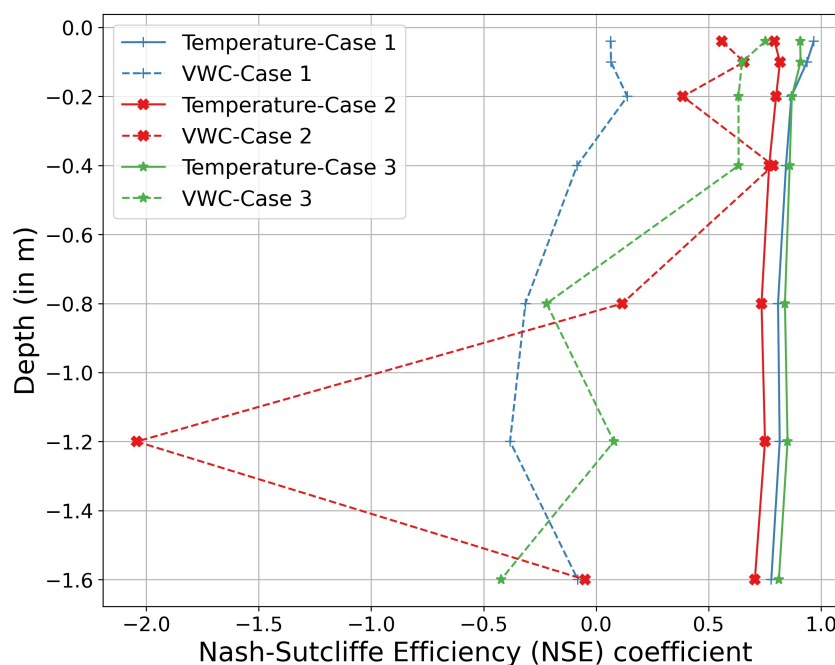
Figure 6. Validation results - Nash Sutcliffe Efficiency Coefficient of subsurface temperature and VWC at depths 0.04 m, 0.2 m, 0.4 m, 0.8 m, 1.2 m, and 1.6 m.

Figure 6 shows the Nash Sutcliffe Efficiency (NSE) coefficient for the three cases at seven depths. The Figure 7 and 8 shows the simulated temperature and VWC along with the energy and water fluxes for the final simulation. These results are very similar to the validation simulation results. Hence, it is referred to the inferences made in this paragraph. The NSE values for VWC are smaller than for temperature because it is difficult to model VWC compared to temperature. Regarding temperature,

275   Case 3 performs best, closely followed by Case 1 and then by Case 2. Generally, the NSE temperature and moisture value reduce with depth, most likely due to the presence of active layer depth and permafrost. The VWC results show that Case 2 and Case 3 perform sufficiently well close to the surface with NSE values greater than 0. However, the NSE values at greater depths are negative because the model could not capture the short periods when the permafrost thaws and the VWC increases. Case 1 NSE moisture values are mostly less than 0 because the increase in VWC due to precipitation input is not represented
280   in the model and permafrost does not thaw in the model.

3.3 Final simulation

3.3.1 Subsurface temperature and Volumetric Water Content (VWC)
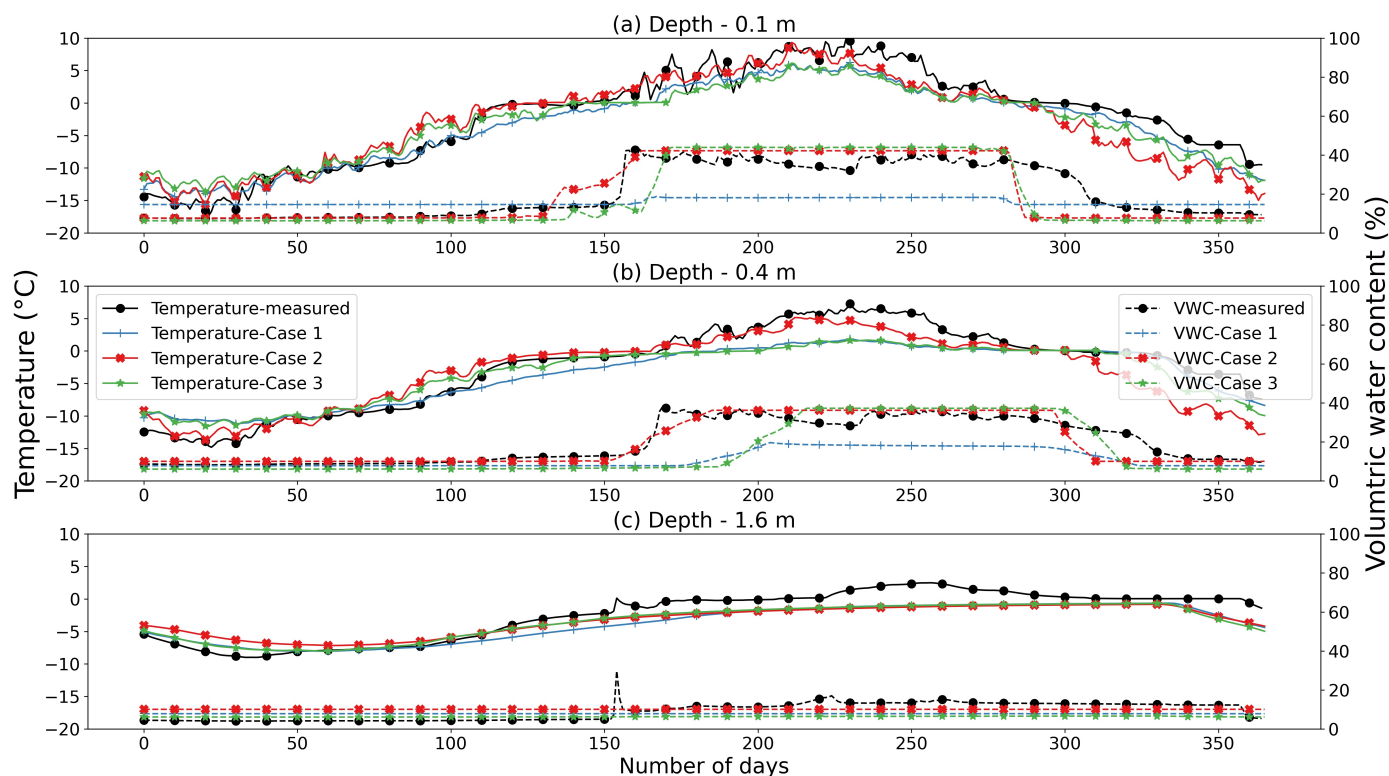
Figure 7. Measured and simulated values of subsurface temperature and VWC at three depths (0.1 m, 0.4 m, and 1.6 m) from the final simulation for Case 1, Case 2, and Case 3.

The results from the final simulations of the three cases with the calibrated parameters are discussed in this section. The results at depths 0.1, 0.4, and 1.6 m are chosen to be presented in Figure 7 because the results are representative of the depth. The
285   top boundary condition for Case 1 was at 0.0 m; therefore, 0.04 m was not considered. The VWC tends to increase during the thaw initiation period (when the temperature increases above 0°C) mainly due to permafrost thaw and reaches the maximum

value during the thawing period. The increase in VWC could also be attributed to the input from precipitation in the variably saturated zone.

Case 1 adequately predicts the temperature close to the surface because the subsurface temperature at 0.0 m is the top boundary condition. However, it under-predicts the temperature mainly during the thawing period because of the absence of an exchange of water fluxes between the atmosphere and subsurface. Because the temperature is under-predicted in Case 1 during the thaw initiation and thawing period, the simulated VWC stays constant (as in depths 0.1 m and 1.6 m) or increases by a smaller amount (as in depth 0.4 m) compared to the measured values. The permafrost thaw depth is under-predicted due to the under-prediction of temperature.

Case 2 predicts plausible temperature values; however, it slightly over-predicts the temperature values during the end of the frozen period and the start of the thaw initiation period. It predicts the soil temperature reasonably well during the thawing period, increasing VWC to reach its maximum value. Nonetheless, it under-predicts the temperature during the freeze initiation and frozen period; hence, the simulated VWC drops quicker than the measured values. The over-prediction and under-prediction of temperature are likely attributed to the absence of snow in Case 2. Snow acts as an insulation layer - prevents the warming during the end of the frozen period and thaw initiation period and cooling of the subsurface during the freeze initiation and start of the frozen period. It could mean that when the simulation is run longer, Case 2 will under-predict the temperature year after year, leading to lesser permafrost thaw.

Case 3 also predicts plausible temperature values; however, it under-predicts the values during the thawing period. Due to snow deposition at the end of the frozen period, the near subsurface experiences a zero-curtain effect (temperatures around 0°C). However, there is a delay in the thawing of the subsurface. Therefore, the VWC increase and permafrost thaw is also delayed. The maximum increase in VWC during the peak thawing period is well-captured. Both Case 2 and Case 3 experience an early freeze initiation period compared to the measured values. This is indicated by the earlier drop in the VWC compared to the measured values. The subsurface temperature remains around 0°C again due to snow deposition. Case 3 also under-predicts the temperature during the frozen period, although it is closer to the measured values than Case 2.

310 3.3.2 Surface energy and water balance
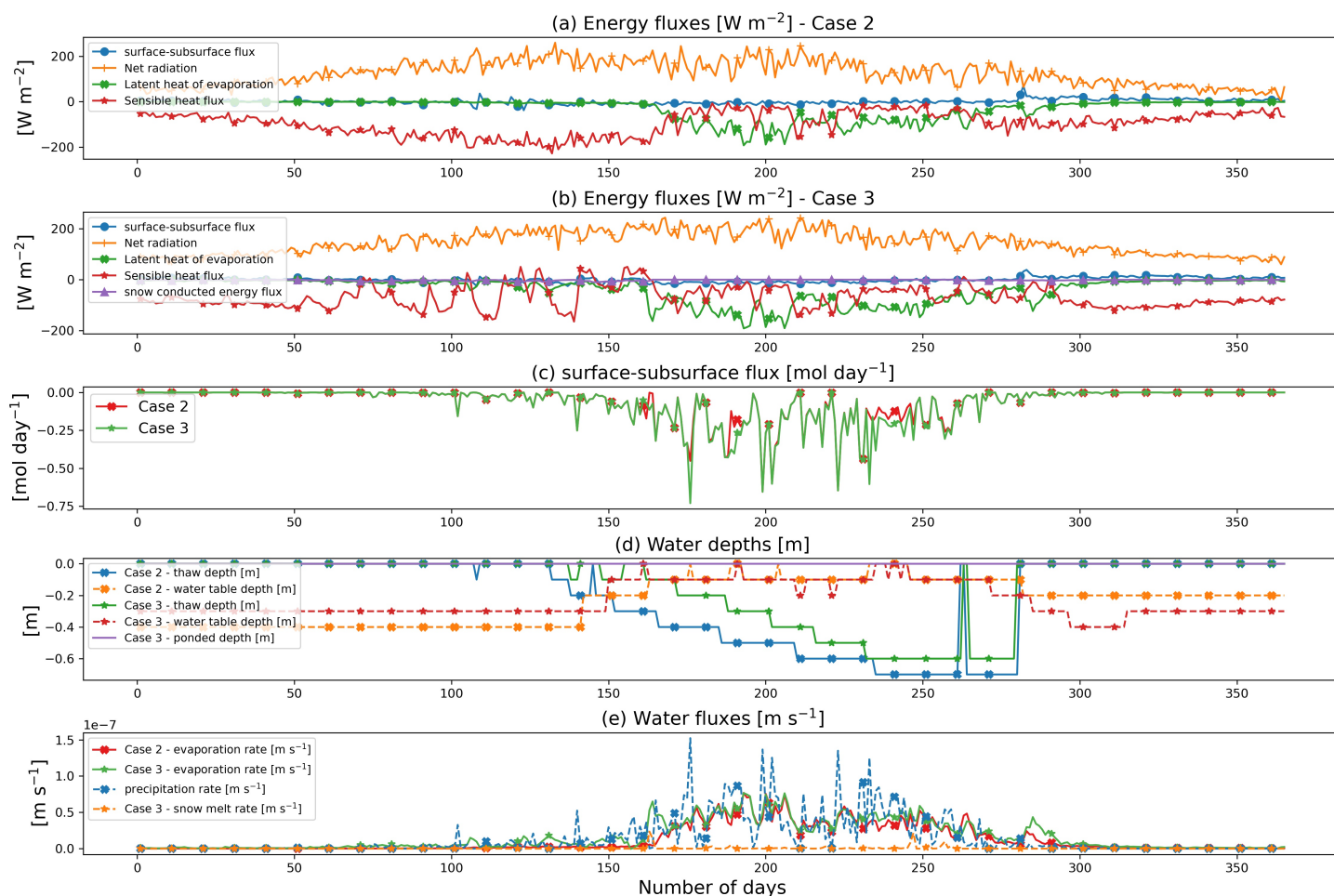
Figure 8. The water and energy fluxes at the surface-subsurface interface from the final simulation for Case 2 and Case 3. Panels (a) and (b) show the energy fluxes: surface-subsurface energy flux, net radiation, latent heat of evaporation, and sensible heat flux. The panel (c) shows the surface-subsurface water flux. Panel (d) shows the water depths: thaw depth, water table depth, and ponded depth. Panel (e) shows the water fluxes: evaporation rate, precipitation rate, and snow melt rate. Net radiation is the summation of incoming and outgoing shortwave and longwave radiation.

Figure 8 represents the water and energy fluxes at the surface-subsurface interface for Case 2 and Case 3. Case 1 was not shown in this figure because there are no surface-subsurface water and energy fluxes. When the fluxes are positive, they are transferred from the subsurface to the surface system.

For Case 2, the net radiation and sensible heat flux gradually increase during the frozen period because shortwave radiation
315 and wind speed increase, respectively. The surface-subsurface water flux, water table depth, and thawed depth remain constant as there is no incoming water flux or thawing. During the thaw initiation period, the net radiation and sensible heat flux continue

to increase, and the surface-subsurface water flux rises due to the increased precipitation rate. The thaw depth also increases; however, the surface energy flux is close to 0. During the thawing period, the sensible heat flux and water table depth reduce; the surface-subsurface flux, evaporation rate, and thaw depth increase due to increased precipitation. The surface-subsurface energy flux remains more or less close to 0. Hence, we can interpret that the rise in thaw depth is likely due to the combined effect of the heat imparted from the advected liquid water, the change in thermal conductivity of the subsurface due to infiltration and latent heat. The higher thermal conductivity of wet soil results in more heat conduction within the subsurface. The observed increase in soil water content after rainfall and the influence of convection of liquid water was also reported by others (Kumar et al., 2016; Zhang et al., 2016). The freeze initiation period is characterized by a gradual decrease in net radiation, evaporation rate, water table depth, a sudden drop in active layer depth, and an increase in sensible heat flux. This is associated with decreasing incoming shortwave radiation and precipitation rates.

For Case 3, snow precipitation mainly occurs during the frozen, thaw initiation, and freeze initiation periods, with a significant amount during the thaw initiation period. The net radiation, latent heat of evaporation, and the surface-subsurface flux behave similarly to Case 2. Only during snow melt a slight variation of these variables compared to Case 2 is observed. During snow precipitation in the thaw initiation period, the sensible heat flux decreases, and the evaporation rate increases due to the deposition of snow. The deposited snow melts during the end of the thaw initiation period, causing an increase in the thaw depth. The energy imparted for melting snow results in a lesser amount of surface-subsurface heat flux. Therefore the thaw depth in Case 2 is higher than in Case 3. During the thawing period, the thaw depth reaches a maximum value of 0.6 m. As the net radiation decreases, the active layer freezes, which is indicated by the decrease in the thaw depth and increase in water table depth. Case 3 also shows higher evaporation rates compared to Case 2 since more water is available due to snow deposition.

4 Conclusion

Previous numerical studies on permafrost applied in the QTP have adequately represented permafrost dynamics (Hu et al., 2015; Zhou et al., 2013; Huang et al., 2020b; Zhang et al., 2016). However, the applied top boundary conditions to represent the atmospheric and surface processes were not always justified. Therefore, we have developed, calibrated, validated, and compared three numerical models with increasing surface process complexity. Calibration results showed that permeability and Van Genuchten alpha of peat and mineral were highly sensitive, as also observed in the study by Albers et al. (2020b). The hydraulic parameters were more sensitive than the thermal parameters, probably due to the difficulty in simulating VWC compared to soil temperature. On comparing the three numerical models, we can conclude that

- Considering only subsurface processes is insufficient to simulate active layer development. However, a surface energy and water balance approach requires a large amount of continuous datasets (Ling and Zhang, 2004), which might not be available in data-scarce regions such as the QTP. The numerical model can use an unrealistic parameter dataset that does not represent site-specific conditions to match the calibration targets.

– Liquid precipitation plays a significant role in permafrost degradation. Lamontagne-Hallé et al. (2020) highlights that heat advection through liquid water flow significantly contributes to permafrost degradation. The thermal conductivity of wet soils is greater than that of dry soils. Therefore, the atmospheric-surface-subsurface heat exchange increases with liquid precipitation during the thawing period.

– The insulation effect of snow during the thaw initiation period reduces the maximum active layer depth developed during the end of the thawing period. The deposited snow on the surface leads to a zero-curtain effect; therefore, the subsurface remains around 0°C, protecting the permafrost from thawing (Zhou et al., 2013).

We successfully established a calibrated and validated pseudo-1-D model at the Yakou catchment. A novel methodology is also proposed to assess the surface process level complexity in permafrost-dominated regions. The PEST calibration was performed once for each case, implying that the highly parameterized calibrated dataset is non-unique. Different initial parameter sets and bounds with non-physical ranges can be tested to assess the uniqueness of parameters (Albers et al., 2020b). Snowdrift and groundwater movement was not tested since a pseudo-1-D model was considered. The methodology could be retested with a more extended input period and field-determined parameters at the Yakou catchment. A similar procedure can be employed in other permafrost regions to evaluate the surface process level complexity and to calibrate and validate the numerical model, provided that a sufficient amount of datasets are available. The calibrated and validated 1-D model can be used to assess the influence of climate change on permafrost in the future. The results from the impacts of climate change on permafrost may provide evidence of permafrost degradation and initiate the discussion on developing mitigation strategies.

365 ## 5   Nomenclature

Symbols	Description	Units
A	Surface cell area	[m^2]
$C_{v,soil}$	Volumetric heat capacity of the soil solid material	[J/m$^3 \cdot$ K]
k	Absolute permeability tensor	[m^2]
k_r	Relative permeability	[-]
E	Evaporation/condensation rate	[m/s]
h	Specific enthalpy	[J/mol]
I	Infiltration rate	[mol/s]
μ	Dynamic viscosity	[Pa $\cdot$ s]
n_{depth}	Vertical depths of measurement	[m]
n_{days}	Number of days	[days]
p_l	Liquid pressure	[Pa]
P	Total precipitation rate [rain and snow]	[m/s]
Q_c	Conduction of heat	[W/m^2]
Q_e	Latent heat	[W/m^2]
Q_E	Thermal energy source/sink from the surface	[W/m^3]
Q_{gs}	Net energy flux density into the subsurface	[W/m^2]
Q_h	Sensible heat	[W/m^2]
Q_{lw}^{In}	Incoming longwave radiation	[W/m^2]
Q_{lw}^{Out}	Outgoing longwave radiation	[W/m^2]
$Q_{sw,met}^{In}$	Incoming shortwave radiation	[W/m^2]
R	Runoff	[mol/s]
s	Phase saturation index	[-]
S_m	Measured VWC	[-]
S_s	Simulated VWC	[-]
subscript i	Solid ice	[-]
subscript l	Liquid	[-]
subscript g	Gas	[-]
t	Time	[days]
t_f	Final time	[days]
T	Subsurface temperature	[K]
T_{gs}	Ground surface temperature	[K]
T_m	Measured subsurface temperature	[K]
T_s	Simulated subsurface temperature	[K]
T_{ss}	Snow surface temperature	[K]
θ_s	Surface water content	[mol]
u	Specific internal energy	[J/mol]
V_l	Darcy velocity	[m/s]
$\bar{V}_o$	Mean of the observed variable	[°C or -]
V_m^t	Modeled variable (Temperature or VWC)	[°C or -]
V_o^t	Observed variable (Temperature or VWC)	[°C or -]
W_w	Mass source/sink rate from the surface	[mol/m^3 s]
α	Transitional albedo	[-]
χ	Liquid-ice partitioning factor	[-]
η	Molar density of water (solid ice, liquid, gas)	[mol/m^3]
ω	Mole fraction of water (solid ice, liquid, gas)	[-]
ϕ	Porosity	[-]
ϕ_{min}	Objective function	[-]

Code availability.

– Advanced Terrestrial Simulator (ATS): E.T. Coon, M. Berndt, A. Jan, D. Svyatsky, A.L. Atchley, E. Kikinzon, D.R. Harp, G. Manzini, E. Shelef, K. Lipnikov, R. Garimella, C. Xu, J.D. Moulton, S. Karra, S.L. Painter, E. Jafarov, and S. Molins. 2020. Advanced Terrestrial Simulator. U.S. Department of Energy, USA. Version 1.0. Available at https://github.com/amanzi/ats.

– PESTPP: White, Jeremy T., et al. Approaches to highly parameterized inversion: PEST++ Version 5, a software suite for parameter estimation, uncertainty analysis, management optimization and sensitivity analysis. No. 7-C26. US Geological Survey, 2020. The code is available at https://github.com/usgs/pestpp

– PEST: Doherty, John.Calibration and uncertainty analysis for complex environmental models. Brisbane, Australia: Watermark Numerical Computing, 2015. The code is available at https://pesthomepage.org/downloads

– The three coupled ATS + PEST models with all the relevant material for simulations is uploaded in a private Github repository: https://github.com/radhakrishnabl96/datamshapratirupa.git. It will be shared based on request.

Data availability.

– Liu, S., Che, T., Xu, Z., Zhang, Y., Tan, J., Ren, Z. (2021).Qilian Mountains integrated observatory network: Dataset of Heihe integrated observatory network (automatic weather station of Yakou station, 2020). National Tibetan Plateau Data Center, DOI: 10.11888/Meteoro.tpdc.271398 .

– Liu, S., Che, T., Xu, Z., Zhang, Y., Tan, J., Ren, Z. (2020).Qilian Mountains integrated observatory network: Dataset of Heihe integrated observatory network (automatic weather station of Yakou station, 2019). National Tibetan Plateau Data Center, DOI: 10.11888/Meteoro.tpdc.270678 .

– Liu, S., Li, X., Che, T., Xu, Z., Zhang, Y., Tan, J. (2019). Qilian Mountains integrated observatory network: Dataset of Heihe integrated observatory network (automatic weather station of Yakou station, 2018). National Tibetan Plateau Data Center, DOI: 10.11888/Meteoro.tpdc.270769.

– Che, T., Liu, S., Li, X., Xu, Z., Zhang, Y., Tan, J. (2019). Observation of water and heat flux in alpine meadow ecosystem - automatic weather station of Yakou station (2015-2017). National Tibetan Plateau Data Center, DOI: 10.11888/Meteoro.tpdc.270279.

– Xiao, Xiong, et al. "Hydrological functioning of thawing soil water in a permafrost-influenced alpine meadow hillslope." Vadose Zone Journal 19.1 (2020): e2022.

– Xiao, Xiong, et al. "Changes in plot-scale runoff generation processes from the spring–summer transition period to the summer months in a permafrost-dominated catchment."Journal of Hydrology 587 (2020): 124966.

395 *Code and data availability.* The code used for the analysis was obtained from the repository developed by RBL.

Reference: (Bangalore Lakshmiprasad, 2023)

Link: https://github.com/radhakrishnabl96/datamshapratirupa.git

400 **Appendix A: Equations**

Above-surface energy and water balance equations: The above-surface energy balance considers two conditions: with snow and without snow, where the primary unknowns are snow surface temperature (T_{ss}) and ground surface temperature (T_{gs}), respectively. The surface energy balance equation with snow is given by (Atchley et al., 2015):

$$0 = (1-\alpha)Q_{sw,met}^{In} + Q_{lw}^{In} + Q_{lw}^{Out}(T_{ss}) + Q_h(T_{ss}) + Q_e(T_{ss}) + Q_c(T_{ss}) \tag{A1}$$

405 where $Q_{sw,met}^{In}$ [W m^{-2}] is the incoming shortwave radiation, Q_{lw}^{In} [W m^{-2}] is the incoming longwave radiation, Q_{lw}^{Out} [W m^{-2}] is the outgoing longwave radiation, Q_h [W m^{-2}] is the sensible heat, Q_e [W m^{-2}] is the latent heat, and Q_c [W m^{-2}] is the conduction of heat from the snow surface through the snowpack to the ground surface. The equation without snow calculates the net energy flux density into the subsurface Q_{gs} [W m^{-2}] and is given by (Atchley et al., 2015):

$$Q_{gs} = (1-\alpha)Q_{sw,met}^{In} + Q_{lw}^{In} + Q_{lw}^{Out}(T_{gs}) + Q_h(T_{gs}) + Q_e(T_{gs}) \tag{A2}$$

410 The dynamic surface in cold regions can simultaneously be covered by snow, ice, ponded water, and tundra vegetation, which is incorporated in ATS through a transitional albedo (α [-]) (refer to equations B8 and B9 (Atchley et al., 2015)). ATS also considers the aging of snow by increasing snow density with time; and by decreasing albedo (refer to equations B6 and

B7 (Atchley et al., 2015)). The calculated albedo value influences the outgoing shortwave radiation. The incoming and outgoing longwave radiation are calculated based on air and surface emissivity and temperature, respectively (refer to equations B3 and

415 B21 (Atchley et al., 2015)). The sensible heat depends on vegetation, wind speed, and temperature difference between surface and air (refer to equation B20 (Atchley et al., 2015)). The latent heat depends on the available water on the surface, evaporative resistance, and surface properties (refer to equation B 22 (Atchley et al., 2015)).

The surface water balance equation is given by

$$\frac{d\theta_s}{dt} = P n_l A - I - R - E n_l A \tag{A3}$$

420 where $\frac{d\theta_s}{dt}$ is the change in surface water storage, θ_s [mol] is the surface water content, η_l [mol m^{-3}] is the molar density of liquid, A [m^2] is the surface cell area, P [m s^{-1}] is the total precipitation rate [rain and snow], I [mols^{-1}] is the infiltration rate, R [mol s^{-1}] is the runoff, and E [m s^{-1}] is the evaporation/condensation rate.

Overland energy and flow equations: The shallow overland flow and energy processes are modeled using a combination of the diffusion wave equation and the kinematic wave equation. The liquid-ice partitioning factor χ $[-]$ defines the overland

425 flow equation in non-isothermal conditions. It varies from zero to one and depends on the surface temperature as it increases from the freezing temperature. The readers are referred to section 4 and equations 13, 14, and 15 in the article Painter et al. (2016).

Subsurface energy and flow equations: The primary variables for the subsurface energy and flow equations are subsurface temperature (T [K]) and liquid pressure (p_l [Pa]), respectively. The subsurface energy balance equation is given by (Painter

430 et al., 2016):

$$\frac{\partial}{\partial t}[\phi \sum_{p=i,l,g} (\eta_p s_p u_p) + (1-\phi)C_{v,soil}T] = -\nabla \cdot (\eta_l h_l V_l) + \nabla \cdot (K_e \nabla T) + Q_E \tag{A4}$$

where η_l [mol m^{-3}] is the molar density of liquid, s [-] is the phase saturation index, u [J mol^{-1}] is the specific internal energy, $C_{v,soil}$ [J m^{-3} K^{-1}] is the volumetric heat capacity of the soil solid material, h [J mol^{-1}] is the specific enthalpy, K_e [W m^{-1} K^{-1}] is the equivalent thermal conductivity of soil-water-ice mixture, and Q_E [W m^{-3}] is the thermal energy

435 source/sink from the surface. The subscripts represent solid ice (i), liquid (l), and gas (g), respectively.

A Richards-type approximation models the hydrologic processes with phase change in both saturated and variably saturated conditions as shown in the equation below (Painter et al., 2016):

$$\frac{\partial}{\partial t}[\phi(\omega_g \eta_g s_g + \eta_l s_l + \eta_i s_i)] = -\nabla \cdot [\eta_l V_l] + W_w \tag{A5}$$

Where ϕ [-] is the porosity, ω [-] is the mole fraction of water, and W_w [mol m^{-3} s^{-1}] is the mass source/sink rate from the
440   surface. The mass source/sink rate is determined by the incoming infiltration and outgoing transpiration.

The darcy velocity (V_l [m s^{-1}]) is given by $V_l = -\frac{k_{rl}k}{\mu_l}(\nabla p_l + \rho_l g \hat{z})$ where k [m^2] is the absolute permeability tensor, k_r [-] is the relative permeability, and μ [Pa s] is the dynamic viscosity. Karra et al. (2014) showed that the gas phase can be treated passively for Earth permafrost conditions. Hence the mole fraction of ice phase air and dissolved air is one, i.e., $\omega_i = 1$ and $\omega_l = 1$.

445   The coupling between the subsurface thermal and hydrological processes is achieved by defining three constitutive equations, which represent the relationship between: Soil-freezing curve (Clausius-Clapeyron equation) - temperature and liquid-ice capillary pressure; Permeability function (Van Genuchten Mualem model) - liquid pressure and relative permeability; and thermal property function (BPC model) - liquid pressure and bulk thermal conductivity, and bulk heat capacity (Lamontagne-Hallé et al., 2018). The three equations are physical equations rather than empirical or statistical equations. The Clausius-Clapeyron
450   equation and Van Genuchten Maulem model are given by the equations 1a, 1b, 2a, 2b, and 2c in the article Schuh et al. (2017). The BPC model is shown in the equations A3, A4, A5, and A8 in appendix A of article Atchley et al. (2015).

Appendix B: Data processing

The input and calibration datasets (2015-2020) for the ATS model were acquired from the National Tibetan Plateau Third Pole Environment Data Center (TPDC): from 2015 to 2017 (Che et al., 2019), 2018 (Liu et al., 2019), 2019 (Liu et al.,
455   2020), and 2020 (Liu et al., 2021). The dataset for the year 2015 began on 18-09-2015, and the year 2020 dataset had three months (February - April) of missing data. Therefore, the input dataset of four years from 2016 to 2019 was considered for calibration and validation for Case 1 and Case 2. A five-step procedure was followed for data processing: (i) Selecting input and calibration datasets, (ii) Calculating daily average values, (iii) Identifying and replacing missing values, (iv) Converting units, (v) Plausibility checking.

460   The input datasets are wind speed at 10 m, air temperature at 5 m, liquid precipitation at 10 m, relative humidity at 5 m, incoming shortwave radiation, surface temperature at 0.0 m, and solid precipitation. The selected calibration datasets are soil temperature and VWC at 0.04 m, 0.1 m, 0.2 m, 0.4 m, 0.8 m, 1.2 m, and 1.6 m because they represent the water and heat systems in the subsurface. For the second step, the 10-minute measured dataset was resampled to find the daily average value except for precipitation. We resampled the liquid precipitation values to determine the daily sum because the sensor measures
465   values only when liquid precipitation occurs.

The third step was identifying and replacing missing values. The incoming shortwave radiation contained missing values from 2019-11-01 to 2019-12-31. Wind speed, air temperature, and relative humidity had missing values from 2019-12-12 to 2019-12-24. These missing values were replaced with the previous year's values on the same day. Soil temperature and VWC had no erroneous or missing data from 2016 to 2019. Hence, the data was directly stored and used as calibration data. The
470   solid precipitation [snow] was processed separately. A total of 36 missing values were identified from 2017-10-20 to 2017-11-24. On observing a similar dataset in December 2016, we replaced the missing values with the average snow precipitation in December.

The fourth step was to convert all input parameters to SI units. The air temperature and subsurface temperature at 0.0 cm were converted from °C to Kelvin [1 Kelvin = °C + 273.15], precipitation rain was converted from mm day^{-1} to m s^{-1} [1 mm day^{-1}
475   = $\frac{1}{10^3 \cdot 86400}$ m s^{-1}], and precipitation snow was converted from m day^{-1} to m s^{-1} [1 m day^{-1} = $\frac{1}{86400}$ m s^{-1}]. ATS requires the daily snow water equivalent as input into the model. The cumulative effect of the measured snow depth was removed by subtracting the snow depth of each day from the previous day and considering only positive values. Snow water equivalent is the water content obtained from melting a defined snow depth. Because the mass of the sample is the same, whether it is snow or water ($m_{water} = m_{snow}$), the relationship can be expressed in terms of density ($\rho_{water}V_{water} = \rho_{snow}V_{snow}$). Let V_{snow}
480   be the volume of snow in the sample, ρ_{snow} = 40 kg m^{-3} be the density of snow in the sample, V_{water} be the volume of water when the sample melts, ρ_{water} = 1000 kg m^{-3} be the density of water. The Area (A) is constant for both water and snow, then the $V_{water} = A * SWE$ and $V_{snow} = A * Z_s$ where SWE is the snow water equivalent, Z_s is the depth of snow. We can now write the equation as: $SWE = \frac{\rho_{snow} * Z_s}{\rho_{water}}$. ATS requires SWE in m s^{-1}, hence Z_s needs to converted from m day^{-1} to m s^{-1} [1 m day^{-1} = $\frac{1}{86400}$ m s^{-1}].
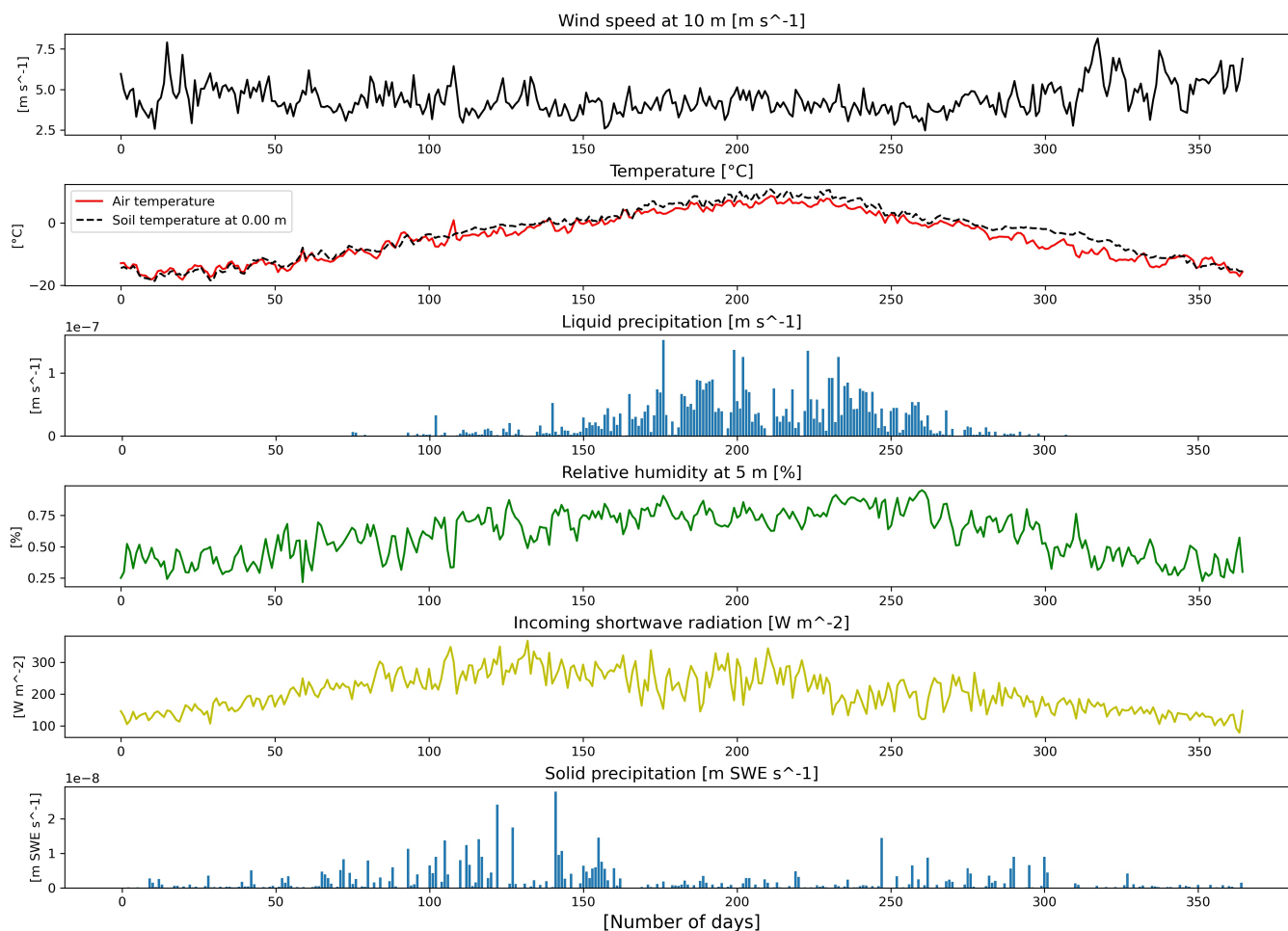
Figure A1. The input parameters for the final simulation represented for one cyclic average year (from top to bottom): Wind speed at 10 m, air temperature at 2 m and soil temperature at 0.0 m, liquid precipitation [rain], relative humidity at 5 m, incoming shortwave radiation, and solid precipitation [snow].

The final step included plotting and visually checking the dataset (refer Figure A1). The measured mean wind speeds, air temperature, liquid precipitation, relative humidity, incoming shortwave radiation, and solid precipitation are 4.435 m s^{-1}, -4.77°C, 1.4796e-08 m s^{-1} (466.6 mm yr^{-1}), 59.81 %, 207.128 W m^{-2}, and 1.9020e-09 m s^{-1} (59.98 mm yr^{-1}) respectively. The wind speeds are higher during the freeze initiation and completely frozen periods than during other periods. The air temperature, relative humidity, and incoming shortwave radiation have a seasonal cycle that reaches a maximum during the thawed period. The liquid precipitation mainly occurs during the monsoon season from May to September (Thaw initiation period to Thawed period). Solid precipitation mainly occurs from March to May, and relatively low values from November to January.

Appendix B: PEST calibration analysis input parameters

Table A1. Initial, lower bound, and upper bounds of parameters for all cases in PEST calibration analysis.

Parameters	Unit	Case 1 - initial	Case 1 - lower bound	Case 1 - upper bound	Case 2 - initial	Case 2 - lower bound	Case 2 - upper bound	Case 3 - initial	Case 3 - lower bound	Case 3 - upper bound
Van Genuchten alpha (peat)	Pa^{-1}	0.010	0.0025	0.0175	0.01	0.0025	0.0125	0.01	0.0025	0.0125
Van Genuchten alpha (mineral)	Pa^{-1}	0.002	0.00045	0.0032	0.002	0.00046	0.0032	0.00182	0.00045	0.0032
Van Genuchten n (peat)	-	2.050	1.025	3.075	1.5	1.025	2.05	1.5	1.025	2.05
Van Genuchten n (mineral)	-	2.050	1.025	3.075	-	-	-	-	-	-
Residual saturation (peat)	-	0.224	0.056	0.393	0.1	0.024	0.2	0.1	0.024	0.2
Residual saturation (mineral)	-	0.160	0.040	0.279	-	-	-	-	-	-
Unfrozen saturated thermal conductivity (peat)	$Wm^{-1}K^{-1}$	0.440	0.110	0.769	-	-	-	-	-	-
Unfrozen saturated thermal conductivity (mineral)	$Wm^{-1}K^{-1}$	0.952	0.238	1.666	-	-	-	-	-	-
Dry thermal conductivity (peat)	$Wm^{-1}K^{-1}$	0.101	0.025	0.177	-	-	-	-	-	-
Dry thermal conductivity (mineral)	$Wm^{-1}K^{-1}$	0.984	0.246	1.723	-	-	-	-	-	-
BPC frozen unsaturated alpha (peat)	-	1.505	0.376	2.634	-	-	-	-	-	-
BPC frozen unsaturated alpha (mineral)	-	1.499	0.375	2.624	-	-	-	-	-	-
BPC unfrozen unsaturated alpha (peat)	-	0.487	0.122	0.852	-	-	-	-	-	-
BPC unfrozen unsaturated alpha (mineral)	-	0.699	0.175	1.223	-	-	-	-	-	-
Porosity (peat)	-	0.637	0.159	1.115	0.637	0.15935	0.85	0.63739	0.159	0.85
Porosity (mineral)	-	0.481	0.120	0.842	0.481	0.12	0.8418	0.481	0.120	0.842
Permeability (peat)	m^2	5.35E-11	1.34E-11	9.35E-11	5.346e-11	1.34E-11	9.3565e-11	5.35E-11	1.34E-11	9.36E-11
Permeability (mineral)	m^2	1e-13	2.5e-14	1.75e-13	1e-13	2.5e-14	1.75e-13	1e-13	2.5e-14	1.75e-13
Density (peat)	kg m^{-3}	900.000	225.000	1575.0	-	-	-	-	-	-
Density (mineral)	kg m^{-3}	1900.000	950.000	2850.0	-	-	-	-	-	-
Bottom boundary condition	°C	-4.7	-10	1	-4.7	-10	1	-4.7	-10	1

Author contributions. RBL and TG carried out formal analysis, methodology development, visualization, and original draft preparation; 495 RBL, TG, and FZ were involved in conceptualization and data curation; TG and FZ assisted in funding acquisition; RBL and ETC were involved in software implementation; RBL, TG, ETC, and FZ carried out reviewing and editing.

Competing interests. The authors declare that they have no conflict of interest.

Acknowledgements. This research is a contribution to the International Research Training Group "Geo-ecosystems in transition on the 500 Tibetan Plateau (TransTiP), funded by Deutsche Forschungsgemeinschaft (DFG grant 317513741/GRK 2309). Special thanks to the staff members of the Institute of Fluid Mechanics and Environmental Physics (Leibniz Universität Hannover) for support with material and guidance. The Open Access Fund of the Leibniz Universität Hannover funded the publication of this article. We thank the TPDC data platform for providing the Yakou meteorological station and geospatial datasets. We also thank the Leibniz University IT Services for

providing cluster systems to run simulations. Special thanks to Felipe Edgardo Silva Monsalves, Maxim-Caroll Nguetsa, and Hong Zhu
(Master's students of Leibniz Universität Hannover) for supporting the research work.

References

Albers, B. M., Molson, J. W., and Bense, V. F.: Parameter sensitivity analysis of a two-dimensional cryo-hydrogeological numerical model of degrading permafrost near Umiujaq (Nunavik, Canada), Hydrogeology Journal, pp. 1–15, 2020a.

Albers, B. M. C., Molson, J. W., and Bense, V. F.: Parameter sensitivity analysis of a two-dimensional cryo-hydrogeological numerical model of degrading permafrost near Umiujaq (Nunavik, Canada), Hydrogeology Journal, 28, 905–919, https://doi.org/10.1007/s10040-020-02112-2, 2020b.

Atchley, A. L., Painter, S. L., Harp, D. R., Coon, E. T., Wilson, C. J., Liljedahl, A. K., and Romanovsky, V. E.: Using field observations to inform thermal hydrology models of permafrost dynamics with ATS (v0.83), https://doi.org/10.5194/gmd-8-2701-2015, 2015.

Bangalore Lakshmiprasad, R.: radhakrishnabl96/datamshapratirupa: Initial release, https://doi.org/10.5281/zenodo.8273589, 2023.

Chang, J., Ye, R., and Wang, G.: Review: Progress in permafrost hydrogeology in China, Hydrogeology Journal, 26, 1387–1399, https://doi.org/10.1007/s10040-018-1802-6, 2018.

Chang, X., Jin, H., Zhang, Y., He, R., Luo, D., Wang, Y., Lü, L., and Zhang, Q.: Thermal impacts of boreal forest vegetation on active layer and permafrost soils in northern Da Xing'anling (Hinggan) Mountains, Northeast China, Arctic, Antarctic, and Alpine Research, 47, 267–279, 2015.

Che, T., Liu, S., Li, X., Xu, Z., Zhang, Y., and Tan, J.: Observation of water and heat flux in alpine meadow ecosystem–automatic weather station of Yakou station2015-2017, https://doi.org/10.11888/Meteoro.tpdc.270279, 2019.

Coon, E. T., Moulton, J. D., and Painter, S. L.: Managing complexity in simulations of land surface and near-surface processes, Environmental Modelling & Software, 78, 134–149, 2016.

Dagenais, S., Molson, J., Lemieux, J.-M., Fortier, R., and Therrien, R.: Coupled cryo-hydrogeological modelling of permafrost dynamics near Umiujaq (Nunavik, Canada), Hydrogeology Journal, 28, 887–904, https://doi.org/10.1007/s10040-020-02111-3, 2020a.

Dagenais, S., Molson, J., Lemieux, J.-M., Fortier, R., and Therrien, R.: Coupled cryo-hydrogeological modelling of permafrost dynamics near Umiujaq (Nunavik, Canada), Hydrogeology Journal, pp. 1–18, 2020b.

Doherty, J.: Calibration and uncertainty analysis for complex environmental models, Watermark Numerical Computing Brisbane, Australia, 2015.

Farr, T. G., Rosen, P. A., Caro, E., Crippen, R., Duren, R., Hensley, S., Kobrick, M., Paller, M., Rodriguez, E., Roth, L., et al.: The shuttle radar topography mission, Reviews of geophysics, 45, 2007.

Frampton, A., Painter, S. L., and Destouni, G.: Permafrost degradation and subsurface-flow changes caused by surface warming trends, Hydrogeology Journal, 21, 271–280, 2013.

Gao, H., Wang, J., Yang, Y., Pan, X., Ding, Y., and Duan, Z.: Permafrost hydrology of the Qinghai-Tibet Plateau: A review of processes and modeling, Frontiers in Earth Science, 8, 576 838, 2021.

Grenier, C., Anbergen, H., Bense, V., Chanzy, Q., Coon, E., Collier, N., Costard, F., Ferry, M., Frampton, A., Frederick, J., et al.: Groundwater flow and heat transport for systems undergoing freeze-thaw: Intercomparison of numerical simulators for 2D test cases, Advances in water resources, 114, 196–218, 2018.

Harp, D. R., Atchley, A. L., Painter, S. L., Coon, E. T., Wilson, C. J., Romanovsky, V. E., and Rowland, J. C.: Effect of soil property
540   uncertainties on permafrost thaw projections: a calibration-constrained analysis, The Cryosphere, 10, 341–358, https://doi.org/10.5194/tc-
       10-341-2016, 2016.

Hu, G., Zhao, L., Li, R., Wu, T., Wu, X., Pang, Q., Xiao, Y., Qiao, Y., and Shi, J.: Modeling hydrothermal transfer processes in permafrost
       regions of Qinghai-Tibet Plateau in China, Chinese geographical science, 25, 713–727, 2015.

Huang, K., Dai, J., Wang, G., Chang, J., Lu, Y., Song, C., Hu, Z., Ahmed, N., and Ye, R.: The impact of land surface temperatures on suprap-
545   ermafrost groundwater on the central Qinghai–Tibet Plateau, Hydrological Processes, 34, 1475–1488, https://doi.org/10.1002/hyp.13677,
       2020a.

Huang, K., Dai, J., Wang, G., Chang, J., Lu, Y., Song, C., Hu, Z., Ahmed, N., and Ye, R.: The impact of land surface temperatures on
       suprapermafrost groundwater on the central Qinghai-Tibet Plateau, Hydrological Processes, 34, 1475–1488, 2020b.

Jafarov, E. E., Coon, E. T., Harp, D. R., Wilson, C. J., Painter, S. L., Atchley, A. L., and Romanovsky, V. E.: Modeling the role of preferential
550   snow accumulation in through talik development and hillslope groundwater flow in a transitional permafrost landscape, Environmental
       Research Letters, 13, 105 006, https://doi.org/10.1088/1748-9326/aadd30, 2018.

Jafarov, E. E., Harp, D. R., Coon, E. T., Dafflon, B., Tran, A. P., Atchley, A. L., Lin, Y., and Wilson, C. J.: Estimation of subsurface porosities
       and thermal conductivities of polygonal tundra by coupled inversion of electrical resistivity, temperature, and moisture content data, The
       Cryosphere, 14, 77–91, https://doi.org/10.5194/tc-14-77-2020, 2020.

555 Jiang, Y., Zhuang, Q., and O'Donnell, J. A.: Modeling thermal dynamics of active layer soils and near–surface permafrost using a fully
       coupled water and heat transport model, Journal of Geophysical Research: Atmospheres, 117, https://doi.org/10.1029/2012JD017512,
       2012.

Kane, D. L., Hinzman, L. D., and Zarling, J. P.: Thermal response of the active layer to climatic warming in a permafrost environment, Cold
       Regions Science and Technology, 19, 111–122, 1991.

560 Karra, S., Painter, S., and Lichtner, P.: Three-phase numerical model for subsurface hydrology in permafrost-affected regions (PFLOTRAN-
       ICE v1. 0), The Cryosphere, 8, 1935–1950, 2014.

Kumar, J., Collier, N., Bisht, G., Mills, R. T., Thornton, P. E., Iversen, C. M., and Romanovsky, V.: Modeling the spatiotemporal variability
       in subsurface thermal regimes across a low-relief polygonal tundra landscape, The Cryosphere, 10, 2241–2274, https://doi.org/10.5194/tc-
       10-2241-2016, 2016.

565 Kurylyk, B. L. and Watanabe, K.: The mathematical representation of freezing and thawing processes in variably-saturated, non-deformable
       soils, Advances in Water Resources, 60, 160–177, https://doi.org/10.1016/j.advwatres.2013.07.016, 2013.

Lamontagne-Hallé, P., McKenzie, J. M., Kurylyk, B. L., and Zipper, S. C.: Changing groundwater discharge dynamics in permafrost regions,
       Environmental Research Letters, 13, 084 017, 2018.

Lamontagne-Hallé, P., McKenzie, J. M., Kurylyk, B. L., Molson, J., and Lyon, L. N.: Guidelines for cold–regions groundwater numerical
570   modeling, WIREs Water, 7, https://doi.org/10.1002/wat2.1467, 2020.

Langford, J. E., Schincariol, R. A., Nagare, R. M., Quinton, W. L., and Mohammed, A. A.: Transient and transition factors in modeling
       permafrost thaw and groundwater flow, Groundwater, 58, 258–268, 2020.

Ling, F. and Zhang, T.: A numerical model for surface energy balance and thermal regime of the active layer and permafrost containing unfrozen water, Cold Regions Science and Technology, 38, 1–15, https://doi.org/10.1016/S0165-232X(03)00057-0, 2004.

575 Liu, S., Li, X., Che, T., Xu, Z., Zhang, Y., and Tan, J.: Qilian Mountains integrated observatory network: Dataset of Heihe integrated observatory network (automatic weather station of Yakou station, 2018), https://doi.org/10.11888/Meteoro.tpdc.270769, 2019.

Liu, S., Che, T., Xu, Z., Zhang, Y., Tan, J., and Ren, Z.: Qilian Mountains integrated observatory network: Dataset of Heihe integrated observatory network (automatic weather station of Yakou station, 2019), https://doi.org/10.11888/Meteoro.tpdc.270678, 2020.

Liu, S., Che, T., Xu, Z., Zhang, Y., Tan, J., and Ren, Z.: Qilian Mountains integrated observatory network: Dataset of Heihe integrated

580 observatory network (automatic weather station of Yakou station, 2020), https://doi.org/10.11888/Meteoro.tpdc.271398, 2021.

McKenzie, J. M., Voss, C. I., and Siegel, D. I.: Groundwater flow with energy transport and water–ice phase change: Numerical simulations, benchmarks, and application to freezing in peat bogs, Advances in water resources, 30, 966–983, 2007.

Moulton, J., Berndt, M., Garimella, R., Prichett-Sheats, L., Hammond, G., Day, M., and Meza, J.: High-level design of Amanzi, the multi-process high performance computing simulator, Office of Environmental Management, United States Department of Energy, Washington

585 DC, 495, 2012.

O'Connor, M. T., Cardenas, M. B., Ferencz, S. B., Wu, Y., Neilson, B. T., Chen, J., and Kling, G. W.: Empirical Models for Predicting Water and Heat Flow Properties of Permafrost Soils, Geophysical Research Letters, 47, https://doi.org/10.1029/2020GL087646, 2020.

Painter, S. L., Coon, E. T., Atchley, A. L., Berndt, M., Garimella, R., Moulton, J. D., Svyatskiy, D., and Wilson, C. J.: Integrated surface/sub-surface permafrost thermal hydrology: Model formulation and proof-of-concept simulations, Water Resources Research, 52, 6062–6077,

590 2016.

Ran, Y., Wang, L., Zeng, T., Ge, C., and Li, H.: One belt, one road" boundary map of key basins in Asia. National Tibetan Plateau Data Center 2020, Proceedings of the 22nd EGU General Assembly, Online, pp. 4–8, 2020.

S.A. Harris, H.M. French, J. H. G. J. B. L. D. S. R. v. E.: Glossary of Permafrost and Related Ground-Ice Terms, National Research Council of Canada Ottawa, Ontario, Canada KIA OR6, 1998.

595 Schuh, C., Frampton, A., and Christiansen, H. H.: Soil moisture redistribution and its effect on inter-annual active layer temperature and thickness variations in a dry loess terrace in Adventdalen, Svalbard, The Cryosphere, 11, 635–651, https://doi.org/10.5194/tc-11-635-2017, 2017.

Stocker, T.: Climate change 2013: the physical science basis: Working Group I contribution to the Fifth assessment report of the Intergovernmental Panel on Climate Change, Cambridge university press, 2014.

600 Voss, C. and Provost, A.: SUTRA: A model for saturated-unsaturated, variable-density groundwater flow with solute or energy transport. USGS Water-Resources Investigations Report, 02-4231, US Geological Survey, Reston, VA, 2010.

Wu, X., Zhao, L., Fang, H., Zhao, Y., Smoak, J. M., Pang, Q., and Ding, Y.: Environmental controls on soil organic carbon and nitrogen stocks in the high-altitude arid western Qinghai-Tibetan Plateau permafrost region, Journal of Geophysical Research: Biogeosciences, 121, 176–187, 2016.

605 Xiao, X., Zhang, F., Li, X., Wang, G., Zeng, C., and Shi, X.: Hydrological functioning of thawing soil water in a permafrost–influenced alpine meadow hillslope, Vadose Zone Journal, 19, https://doi.org/10.1002/vzj2.20022, 2020a.

Xiao, X., Zhang, F., Li, X., Wang, G., Zeng, C., and Shi, X.: Hydrological functioning of thawing soil water in a permafrost-influenced alpine meadow hillslope, Vadose Zone Journal, 19, e20 022, 2020b.

Yongjian, D., Shiqiang, Z., and Rensheng, C.: Cryospheric hydrology: decode the largest freshwater reservoir on earth, Bulletin of Chinese Academy of Sciences (Chinese Version), 35, 414–424, 2020.

Yue, G., Zhao, L., Zhao, Y., Du, E., Wang, Q., Wang, Z., and Qiao, Y.: Relationship between soil properties in permafrost active layer and surface vegetation in Xidatan on the Qinghai-Tibetan Plateau, Journal of Glaciology and Geocryology, 35, 565–573, 2013.

Zhang, G., Yao, T., Shum, C., Yi, S., Yang, K., Xie, H., Feng, W., Bolch, T., Wang, L., Behrangi, A., et al.: Lake volume and groundwater storage variations in Tibetan Plateau's endorheic basin, Geophysical Research Letters, 44, 5550–5560, 2017.

Zhang, M., Wen, Z., Xue, K., Chen, L., and Li, D.: A coupled model for liquid water, water vapor and heat transport of saturated–unsaturated soil in cold regions: model formulation and verification, Environmental Earth Sciences, 75, https://doi.org/10.1007/s12665-016-5499-3, 2016.

Zhou, J., Kinzelbach, W., Cheng, G., Zhang, W., He, X., and Ye, B.: Monitoring and modeling the influence of snow pack and organic soil on a permafrost active layer, Qinghai–Tibetan Plateau of China, Cold Regions Science and Technology, 90-91, 38–52, https://doi.org/10.1016/j.coldregions.2013.03.003, 2013.